

Citation for published version:
Walsh, D, Zhang, J, Regue Grino, M, Dassanayake, R & Eslava, S 2019, 'Simultaneous Formation of FeOx Electrocatalyst Coating within Hematite Photoanodes for Solar Water Splitting', ACS Applied Energy Materials, vol. 2, no. 3, pp. 2043-2052. https://doi.org/10.1021/acsaem.8b02113

DOI:

10.1021/acsaem.8b02113

Publication date: 2019

Document Version Peer reviewed version

Link to publication

This document is the Accepted Manuscript version of a Published Work that appeared in final form in Applied Energy Materials, copyright @ American Chemical Society after peer review and technical editing by the publisher. To access the final edited and published work see https://pubs.acs.org/doi/10.1021/acsaém.8b02113

#### **University of Bath**

#### **Alternative formats**

If you require this document in an alternative format, please contact: openaccess@bath.ac.uk

Copyright and moral rights for the publications made accessible in the public portal are retained by the authors and/or other copyright owners and it is a condition of accessing publications that users recognise and abide by the legal requirements associated with these rights.

**Take down policy**If you believe that this document breaches copyright please contact us providing details, and we will remove access to the work immediately and investigate your claim.

Download date: 09 Mar 2023

Simultaneous Formation of FeO<sub>x</sub> Electrocatalyst
Coating within Hematite Photoanodes for Solar
Water Splitting

Dominic Walsh,\*† Jifang Zhang,† Miriam Regue, §† Ruchi Dassanayake,† and Salvador Eslava\*†

<sup>†</sup>Dept. of Chemical Engineering, University of Bath, Claverton Down, Bath, BA2 7AY, UK.

§ Centre for Sustainable Chemical Technologies, University of Bath, Claverton Down, Bath, BA2 7AY, UK

KEYWORDS. Hematite, photocatalysis, photoelectrochemical, solar water splitting, amorphous iron oxide, lactic acid, photoelectrodes.

ABSTRACT. Depositing an oxygen evolution electrocatalyst on the intricate pores of semiconductor light-absorbing layers of photoanodes for photoelectrochemical solar water splitting is an efficient way to improve their performance, but it adds extra costs and difficulties. In this work, we present a synthesis of hematite ( $\alpha$ -Fe<sub>2</sub>O<sub>3</sub>) photoanodes with a self-derived conductive amorphous FeO<sub>x</sub> electrocatalyst coating. Hematite-FeO<sub>x</sub> photoanodes were prepared via FeOOH precursors modified with low levels of lactic acid additive. In absence of lactic acid, FeOOH consisted of lepidocrocite nanorods that resulted in  $\alpha$ -Fe<sub>2</sub>O<sub>3</sub> particulate

photoanodes with sharp crystal edges upon doctor blading and calcination. Lactic acid addition however resulted in goethite and amorphous FeOOH that formed  $\alpha$ -Fe<sub>2</sub>O<sub>3</sub> particulate photoanodes coated by a thin conductive amorphous FeO<sub>x</sub> layer. Electron microscopies revealed the thickness of this layer was controlled with the addition of lactic acid in the preparation. Photoelectrochemical characterization including Tafel plots, impedance spectroscopy, and hole scavenger measurements confirmed the FeO<sub>x</sub> layer behaved as an FeOOH electrocatalyst enhancing charge transfer efficiency and minimizing electron-hole surface recombination. Such coating and approach increased the electrochemically-active surface area and amount of surface states. Photocurrent increased from 0.32 to 1.39 mA cm<sup>-2</sup> at 1.23 V<sub>RHE</sub> under simulated sunlight, remarkable results for an auto-co-catalyzed and simple solution-process deposition.

## Introduction

The world's energy consumption continues to increase above current ~13 Mtoe levels due to worldwide population growth and economic expansion. To avoid the dependence on fossil fuels, there has been a sharp increase in research and commercialization of solar technologies in the last decade. Among these technologies, the research of photoelectrochemical (PEC) splitting of water to produce hydrogen fuel using low cost components and solar energy calls much attention. <sup>2-4</sup> Candidate metal oxides for the photoanode component of a PEC cell include n-type semiconductors such as TiO<sub>2</sub>, ZnO, WO<sub>3</sub>, and α-Fe<sub>2</sub>O<sub>3</sub> (hematite), being the latter especially promising due to its high elemental abundance, low cost, and solar light absorption properties. <sup>5, 6</sup> For hematite to function effectively as a photoanode, films of a few hundred nanometers thick are required to overcome the low absorption coefficient, whilst nanoscale features better match to short carrier diffusion lengths. <sup>7-14</sup> Materials and production methods that are economically viable and suitable for very large-scale implementation are a key target.

The formation of hematite photoanodes with intricate morphologies and features for water oxidation has been extensively investigated, but more progress is still needed to achieve the maximum theoretical limit of 12.6 mA cm<sup>-2</sup>. 9,15,16 Hematite photoanodes have been prepared with the shape of cauliflowers, nanocones, nanotubes and worms, in attempts to increase the hematite area exposed to the electrolyte and minimize the diffusion path of holes facilitating they reach the electrolyte. 17-20 Some of these approaches require vacuum deposition techniques which can increase costs. Solution processes such as doctor blading or spin coating are inexpensive and can be easily adopted by many researchers and laboratories.

PEC water oxidation is limited by both the high tendency of photoinduced electrons and holes to recombine in the photoanode semiconductor and the poor catalytic properties of semiconductor surfaces to evolve oxygen at the electrolyte interface. The pairing of a semiconductor light absorbing layer with O<sub>2</sub> evolution electrocatalysts that mediate in the oxidation of water and collect the holes to avoid their recombination is a route to significantly enhance photocurrents. Many different electrocatalysts such as Pt, IrO<sub>x</sub>, CoFeO<sub>x</sub>, and CoPi have been directly functionalized on the surface of hematite. They are typically deposited by electrodeposition, drop casting, or more expensive and sophisticated vacuum deposition techniques. This poses an extra deposition step that can increase costs, especially if precious metals are used, and in some cases deteriorate the semiconductor hematite if this is unstable under the deposition conditions. <sup>27, 28</sup>

Herein, we introduce a solution-process method to prepare hematite photoanodes formed simultaneously with a self-derived amorphous surface FeO<sub>x</sub> coating that effectively works as an O<sub>2</sub> evolution electrocatalyst and minimizes losses from surface charge recombination. To generate the amorphous layer we employed the small mono-carboxylated molecule lactic acid [CH<sub>3</sub>CH(OH)COOH, LA] as a biodegradable, non-toxic and low-cost additive in the aqueous

precipitation synthesis of FeOOH nanorod precursors.<sup>29</sup> When these LA-modified FeOOH were readily coated onto transparent conductive supports by doctor blading and heated, simultaneously formation of light-absorbing semiconductor hematite coated with FeO<sub>x</sub> electrocatalyst occurred. This simplified and inexpensive photoanode preparation that self-co-catalyzes with a surface coating reduces costs and boosts photocurrents from 0.32 up to 1.39 mA cm<sup>-2</sup> at 1.23 V<sub>RHE</sub> under simulated sunlight. Electron microscopy confirmed the amorphous layer thickness could be controlled with the levels of LA addition to the solution process. Dark current water oxidations, hole scavenger measurements and a range of photoelectrochemical analysis together showed the amorphous layer was intrinsically more catalytic and suppressed surface electron-hole recombination.

# 2. Experimental Section

#### 2.1 Preparation of FeOOH precursor of hematite films.

100ml of N<sub>2</sub>-degassed distilled water was used to dissolve 0.198g iron (II) chloride tetrahydrate and 0.5406g iron (III) chloride hexahydrate solution (0.02/0.04 M Fe<sup>2+</sup>/Fe<sup>3+</sup>) with stirring.<sup>30</sup> 1M sodium carbonate solution was then added dropwise to the stirred solution until pH rose from 1.8 up to 6, while FeOOH precipitated. The mixture was left to stand for 24 h. Precipitated FeOOH in the presence of LA was alterantively uprepared by adding the equivalent of 0.1, 0.2, 0.3 and 0.4g (0.044 M) of LA (using adjusted weights from an 80% LA solution) to the Fe<sup>2+</sup>/Fe<sup>3+</sup> solution prior to adding dropwise the sodium carbonate. For example 0.2g of LA was equivalent to a 2.73:1 molar ratio of Fe:LA. In all cases, a brown sediment was formed that was washed three times by repeated centrifugation at 3500 rpm for 5 min and redispersion in distilled water. A final 10-min centrifugation was carried out, followed by

removal of the supernatant and addition of 3 ml of ethanol to form brown slurry mixtures that were stored in sealed vials.

2.2 Preparation of PEC photoanode slides. To prepare coated slides suitable for PEC measurements 0.4g FeOOH/ethanol sediments (dry weight 0.025g FeOOH) were mixed with 1 ml of a 2-propanol solution of 0.5wt% acetylacetonate (acac) capping agent and 4wt% polyvinylpyrollidone (Mr 40k, PVP). This mixture was then sonicated for 5 min. An excess of two drops (~0.06ml) of this mixture were placed onto thoroughly cleaned and washed 12 x 25x 1.05 mm<sup>3</sup> fluoridated tin oxide coated aluminoborosilicate glass slides (ABS-FTO, Solaronix, CH) and doctor bladed at 0.20mm layer thickness – an overall setting of 1.25mm including the 1.05 mm thick slide. Then, coatings were allowed to dry in air. The low level of PVP aided formation of regular thin continuous films that adhered firmly to the FTO slides. The slides were then placed directly into a tube furnace pre-heated to 800°C and heated for 20 min followed by immediate removal and cooling to room temperature in air. Previous studies have shown these heating conditions to be optimal for diffusion of Sn into the hematite layer which increases conductivity and raises photocurrent.<sup>14</sup> Apart from Sn diffusion effects, previous studies have shown clearly the ABS-FTO glass is essentially otherwise unaltered by heating at 800 °C.<sup>25,31</sup> The yellow coating of FeOOH material changed into red/orange hematite that was continuous and firmly adhered to the slide surface. The slides were washed in distilled water and air dried. The following reaction took place during the heating at 800°C for 20 min (eq 1):

$$2 \text{ FeOOH} \rightarrow \text{Fe}_2\text{O}_3 + \text{H}_2\text{O} \tag{1}$$

#### 2.3 PEC measurements.

Photocurrent density (in mA cm<sup>-2</sup>), PEC impedance spectroscopy (PEIS), incident photon-to-current efficiency (IPCE) and Faradaic efficiency were investigated in a three-electrode PEC quartz cell. Simulated sunlight on an circular 0.283cm<sup>2</sup> area was supplied by a 300 W Xe Lamp

(LOT Quantum Design) using an AM 1.5G filter (which simulates the terrestrial solar spectrum at ground level). Illumination intensity was set to 1 sun (100 mW cm<sup>-2</sup>) by calibration with a silicon photodiode linked to an ILT1400 Radiometer Photometer. An Ivium Compacstat.h mobile potentiostat was used with IviumSoft version.2.6 software. In the three electrode system, the working electrode was the as-prepared hematite photoanode, the counter electrode a Pt wire, and an Ag/AgCl (in 3.5 M KCl) electrode the reference electrode. 1 M KOH solution (pH 13.9) was used as an electrolyte. The working electrode was illuminated from the back side (glass side). Photocurrent density - potential (J-V) curves were recorded at a scan rate of 20 mV s<sup>-1</sup>. The measured potentials vs. Ag/AgCl (E<sub>Ag/AgCl</sub>) were converted to RHE potential (E<sub>RHE</sub>) following the Nernst equation (eq 2):

$$E_{RHE}^{\circ} = E_{Ag/AgCl}^{\circ} + E_{Ag/AgCl} + 0.059 \text{ pH}$$
 (2)

where  $E_{Ag/AgCl}^{\circ} = +0.205 \text{ V}$ 

In PEIS measurements, a potential perturbation of 10 mV was applied at a frequency range from  $10^5$  to 0.1 Hz. The data were collected at direct current potentiostatic conditions from 0.7 to 1.3  $V_{RHE}$  at a step of 0.05 V and fitted using Zview software (version 3.5, Scribner®). Simulated solar illumination (AM1.5G, 100mW cm<sup>-2</sup>) was used to illuminate the back (glass) faces of the FTO slide supports.

Stability of a  $Fe_2O_3$ - $FeO_x$  (0.2g LA) photoanode was measured over 2.5 h under chopped simulated sunlight at an applied potential of 1.23  $V_{RHE}$ .

Faradaic efficiency was measured in a gas-tight cell under the same previous conditions (AM1.5G, 100mW cm<sup>-2</sup>, 1.23 V<sub>RHE</sub>, 1 M KOH) for 80 min using a Pyroscience Firesting O2 sensor in the head space (more details in the Supporting Information).

#### 2.4. Cyclic voltammetry for surface area

Electrochemically active surface area (ECSA) of photoanodes was investigated using cyclic voltammetry (CV), scanning from 0 to 0.17  $V_{Ag/AgCl}$  at scan rates between 10 and 200 mV s<sup>-1</sup>, in 1 M KOH solution (pH =13.9).<sup>32</sup> ECSA is proportional to the double layer capacitance ( $C_{dl}$ ), which is estimated from the slope of the plot  $\Delta J$  vs. scan rate and dividing by two.<sup>33</sup>  $\Delta J$  is equal to ( $J_a$ – $J_c$ ), where  $J_a$  and  $J_c$  are the anodic and cathodic current densities, respectively, in this case taken at 0.1  $V_{Ag/AgCl}$  in the CV scans.<sup>34,35</sup> Sample slides were measured in triplicate and consistent  $C_{dl}$  values were obtained.

#### 2.5. Hole scavenger measurements.

Underlying differences in charge transport properties and surface catalytic properties between samples prepared with different LA levels were studied by adding 0.5 M H<sub>2</sub>O<sub>2</sub> as a hole scavenger into the 1 M KOH electrolyte to eliminate surface recombination.<sup>36</sup>

#### 2.6. Further characterization.

Samples analyzed by powder X-ray diffraction (XRD) were recorded on a Bruker D8 powder diffractometer. FeOOH samples were dried in air and lightly ground by hand before measurement. Hematite photoanodes did not need any preparation for XRD. Crystal modelling and powder XRD diffraction pattern calculation were obtained with Crystalmaker 10.1.1 and CrystalDiffract 6.7.2 software, respectively, and using published crystal structure cif files. Field-emission scanning electron microscopy (FESEM, JEOL JSM-6301F) was employed to observe photo-electrode surfaces and cross-sectional morphology and determine film particle sizes. Samples were not coated before SEM observation. Energy dispersive X-ray spectroscopy (EDXS) was conducted on a JEOL JSM-6480LV SEM at low magnification (~250µm diameter sample area) for elemental composition (for elements heavier than N). Transmission electron

microscopy (TEM) was carried on a JEOL 2100 Plus to characterize the morphology of the samples, the presence of amorphous material, and the lattice fringes of hematite crystals (using ImageJ). FeOOH samples onto carbon-coated copper TEM grids were prepared from suspensions diluted in 2-propanol followed by brief sonication, drop casting and drying. Samples of hematite photoanodes for TEM imaging were prepared by carefully scraping hematite material from the ABS-FTO slide into 2-propanol, followed by brief sonication. Then, one drop of suspension was placed onto the TEM grid and air dried before TEM analysis. UV-Visible spectroscopy of photoanode slides was conducted by diffuse reflectance light absorption measurements on an Agilent UV/Vis Cary 100 spectrometer fitted with a diffuse reflection integrating sphere. Tauc plots were carried out to calculate direct and indirect band gap, using exponents n=2 and n=1/2, respectively (more details in the Supporting Information). Raman spectroscopy was conducted with a Renishaw inVia system utilizing a 532nm laser operating at 0.7mW. Hematite photoanode slides were also analyzed by X-ray photoelectron spectroscopy (XPS) on a Thermo Fisher Scientific K-alpha<sup>+</sup> spectrometer using a microfocused monochromatic Al x-ray source (72 W) over an area of approximately 400 microns. Data was recorded at pass energies of 150 eV for survey scans and 40 eV for high resolution scan with 1 eV and 0.1 eV step sizes respectively. Data analysis was performed in CasaXPS using a Shirley-type background and Scofield cross sections, with an energy dependence of -0.6. Charge neutralization of the sample was achieved using a combination of both low energy electrons and argon ions.

## 3. Results and discussion

#### 3.1 XRD and Raman spectroscopy measurements.

Powder XRD analysis was conducted of FeOOH precipitated from iron chlorides with sodium carbonate solutions. Samples showed broad reflections corresponding to  $\gamma$ -FeOOH,

lepidocrocite (L) (ICDD 74-1877) and a low level of  $\alpha$ -FeOOH, goethite (G) (ICDD 29-713) (Figure 1a). Enhanced  $\gamma$ -FeOOH (X00) reflections could be observed compared to calculated standards. LA was selected as a mild binding agent that could potentially alter the morphology of the precipitated FeOOH and its surface properties, but without strongly chelating or sequestering Fe ions that would lead to entirely amorphous material.  $^{37-39}$  With 0.1g of added LA to the carbonate precipitation process, XRD reflections consisted of poorly crystalline  $\gamma$ -FeOOH (Figure 1b). At 0.2 and 0.3g LA addition, poorly crystalline  $\gamma$ -FeOOH/ $\alpha$ -FeOOH was obtained, with a lower  $\gamma$ -FeOOH proportion at 0.3 g LA addition (Figure 1c,d). At 0.4g LA addition, near amorphous  $\alpha$ -FeOOH was formed (Figure 1e).

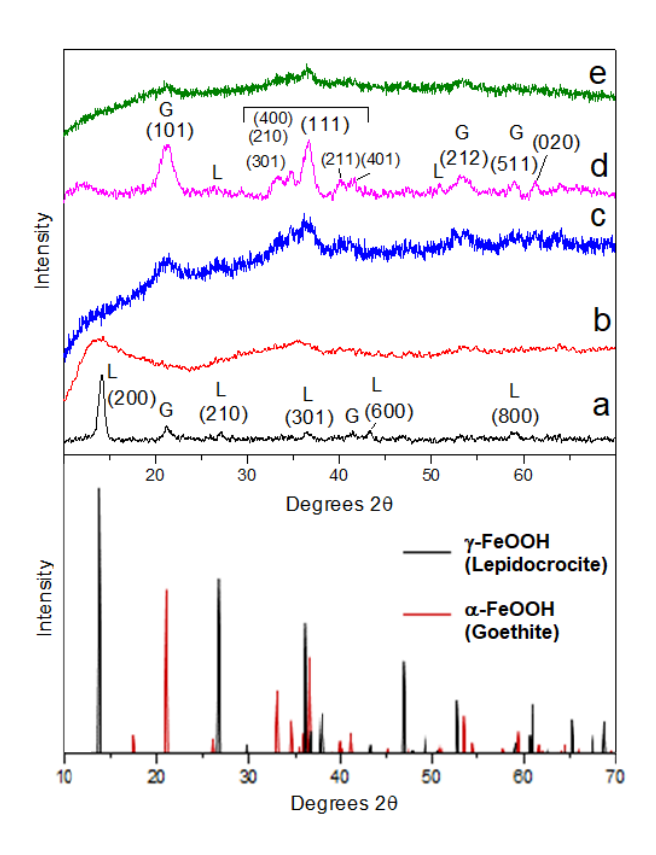


Figure 1. XRD patterns of FeOOH prepared using different amounts of LA. (a) 0 g LA; (b) 0.1 g LA; (c) 0.2 g LA; (d) 0.3 g LA and (e) 0.4g LA. Calculated standards are shown in the bottom for comparison. L and G indicate lepidocrocite (γ-FeOOH) and goethite (α-FeOOH), respectively. (Patterns (d) was smoothed to aid peak assignment).

Raman spectra of dry powder samples prepared in absence of LA match to a modified  $\gamma$ -FeOOH and a  $\beta$ -FeOOH (schwertmannite) like phase, <sup>40</sup> again suggesting some interaction with carbonate anion. With increasing LA usage, a transition was observed from a mixture high in  $\gamma$ -FeOOH and low in  $\alpha$ -FeOOH to the reverse composition (Figure S1). Band assignments and comparison to database standards are shown in Table S1. <sup>41,42</sup> This phase change may be caused by LA interaction with  $\alpha$ -FeOOH planes resulting in increased expression and promotion of this phase over  $\gamma$ -FeOOH. Carboxyl adsorption to  $\alpha$ -FeOOH (100) has been suggested by computational study. <sup>43</sup>

XRD analysis of the photoanode slides prepared by doctor blading FeOOH powders and heating to 800 °C showed reflections corresponding to rhombohedral α-Fe<sub>2</sub>O<sub>3</sub> hematite (ICDD 24-0072), together with strong reflections due to the FTO underlayer (Figure 2). Reflections due to other phases such as Fe<sub>3</sub>O<sub>4</sub> were not observed. Relative reflection intensities with increasing LA use were complex due to differences in thickness of the hematite layer and increasing amorphous FeOOH levels in the precursor. However, it was notable the difference in the relative higher intensity of the (110) compared to the (104) reflection. The (110):(104) ratios of the integrated peak areas were 1: 0.67, 1.24:1, 1.27:1, 1.04:1, 0.49:1 for Fe<sub>2</sub>O<sub>3</sub> (0 g LA), Fe<sub>2</sub>O<sub>3</sub>-FeO<sub>x</sub> (0.1 g LA), Fe<sub>2</sub>O<sub>3</sub>-FeO<sub>x</sub> (0.2 g LA), Fe<sub>2</sub>O<sub>3</sub>-FeO<sub>x</sub> (0.3 g LA), and Fe<sub>2</sub>O<sub>3</sub>-FeO<sub>x</sub> (0.4 g LA), respectively. It is probable that the hematite (110) originates from moderate atomic re-organization of the α-FeOOH (111) plane upon heating and dehydration to hematite. Recently it has been shown that water splitting efficiency of hematite can be substantially increased by enhancement of the (110) crystal orientation due to increased charge transport along this iron rich direction and/or lowered overpotentials (Figure S2).<sup>44,45</sup>

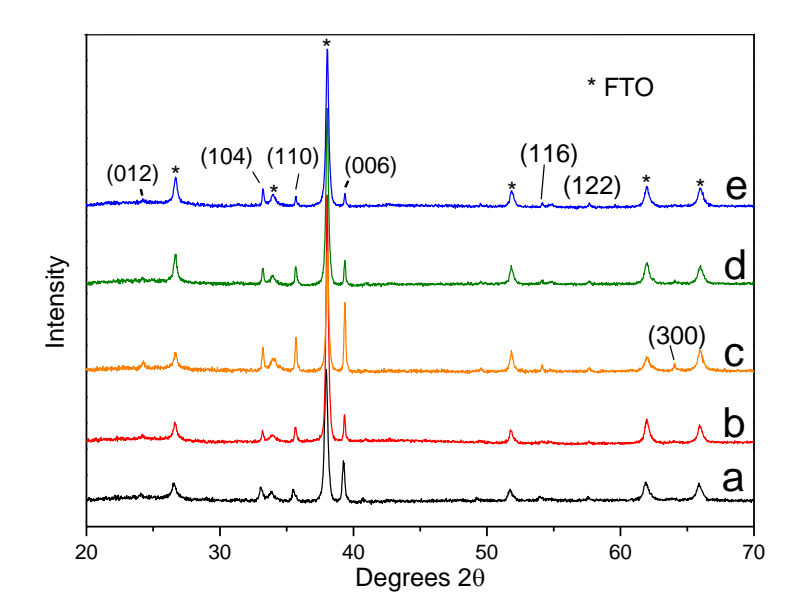


Figure 2. XRD patterns of hematite photoanodes prepared with FeOOH powders synthesized with different levels of LA. (a) Fe<sub>2</sub>O<sub>3</sub> (0g LA); (b) Fe<sub>2</sub>O<sub>3</sub>-FeO<sub>x</sub> (0.1g LA); (c) Fe<sub>2</sub>O<sub>3</sub>-FeO<sub>x</sub> (0.2g LA); (d) Fe<sub>2</sub>O<sub>3</sub>-FeO<sub>x</sub> (0.3g LA); (e) Fe<sub>2</sub>O<sub>3</sub>-FeO<sub>x</sub> (0.4g LA). Starred peaks indicate diffraction from FTO.

**3.2. Electron microscopy.** TEM showed that FeOOH precipitated in the absence of LA generated rod crystals of 20-50 nm in length and 10 nm in width (Figure 3a-f). Narrowing of the needle-shaped crystals with increasing LA was evident along with presence of increasing levels of ill-defined amorphous material.

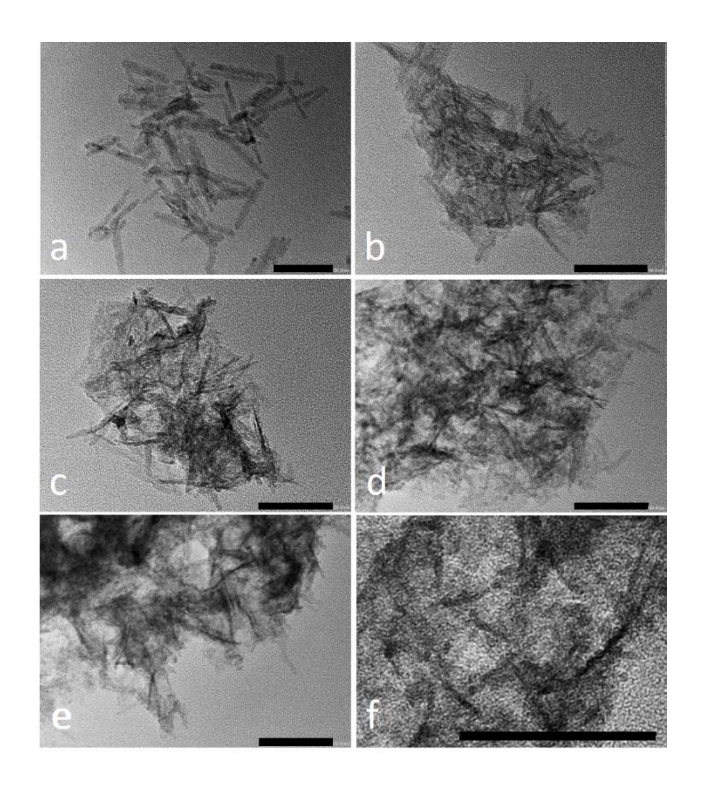


Figure 3. TEM micrographs of FeOOH powders prepared with different levels of LA. (a) 0g LA; (b) 0.1g LA; (c) 0.2g LA; (d) 0.3gLA; (e) 0.4g LA; and (f) 0.4g LA, zoomed in. Scale bar: 50 nm

Cross sectional FESEM micrographs of resulting photoanodes showed the hematite crystal layer firmly bound to the FTO (Figure S3). Hematite layer thicknesses varied from 275 to 400 nm, due to subtle differences in the mixture concentration and doctor blading process. FESEM of the top surface of photoanodes prepared with FeOOH in absence of LA showed irregular blocks of hematite size crystals (~50-200 nm) that were often fused together (Figure 4a). No notable differences can be observed for different levels of LA use, except for LA ≥0.3 g which led to a reduced number of crystals formed but more coupled and larger (Figure 4d,e). A significant feature in the FESEM micrographs was the appearance of a continuous coating upon linked crystals with the use of LA (note loss of sharpness in Figure 4b-e insets). The lower contrast of the coating layer is suggestive of lower density and/or better conductivity. This

coating was confirmed by TEM imaging. Fragments of the hematite photoanodes showed a sharp crystal edge with no LA use (Figure 4f and S4). With the use of LA, hematite crystals are however terminated with an amorphous coating absent of lattice fringes and of lower density. The average coating thickness was 5-10 nm for Fe<sub>2</sub>O<sub>3</sub>-FeO<sub>x</sub> (0.2 g LA) and 10-20 nm for Fe<sub>2</sub>O<sub>3</sub>-FeO<sub>x</sub> (0.4 g LA) (Figure 4g-h and S4). Also visible in the Fe<sub>2</sub>O<sub>3</sub>-FeO<sub>x</sub> (0.4g LA) sample, were occasional graphitic carbon layers between the crystalline hematite and amorphous FeO<sub>x</sub> layer and in smaller amount at the surface of the amorphous FeO<sub>x</sub> layer (arrowed in Figure 4h). Since graphitic carbon was only observed for Fe<sub>2</sub>O<sub>3</sub>-FeO<sub>x</sub> (0.4g LA) which had an excess of LA, we assign this graphitic carbon to the decomposition of LA and its trapping in the structure. Samples were heated at 800 °C, but they were only kept at this temperature for 20 min. Graphitic carbon on hematite has previously been observed on certain preparation conditions. <sup>46</sup> In any case, the amount of graphitic carbon was very low compared with the presence of amorphous FeO<sub>x</sub> surrounding hematite crystals and no parasitic absorption due to carbon could be observed.

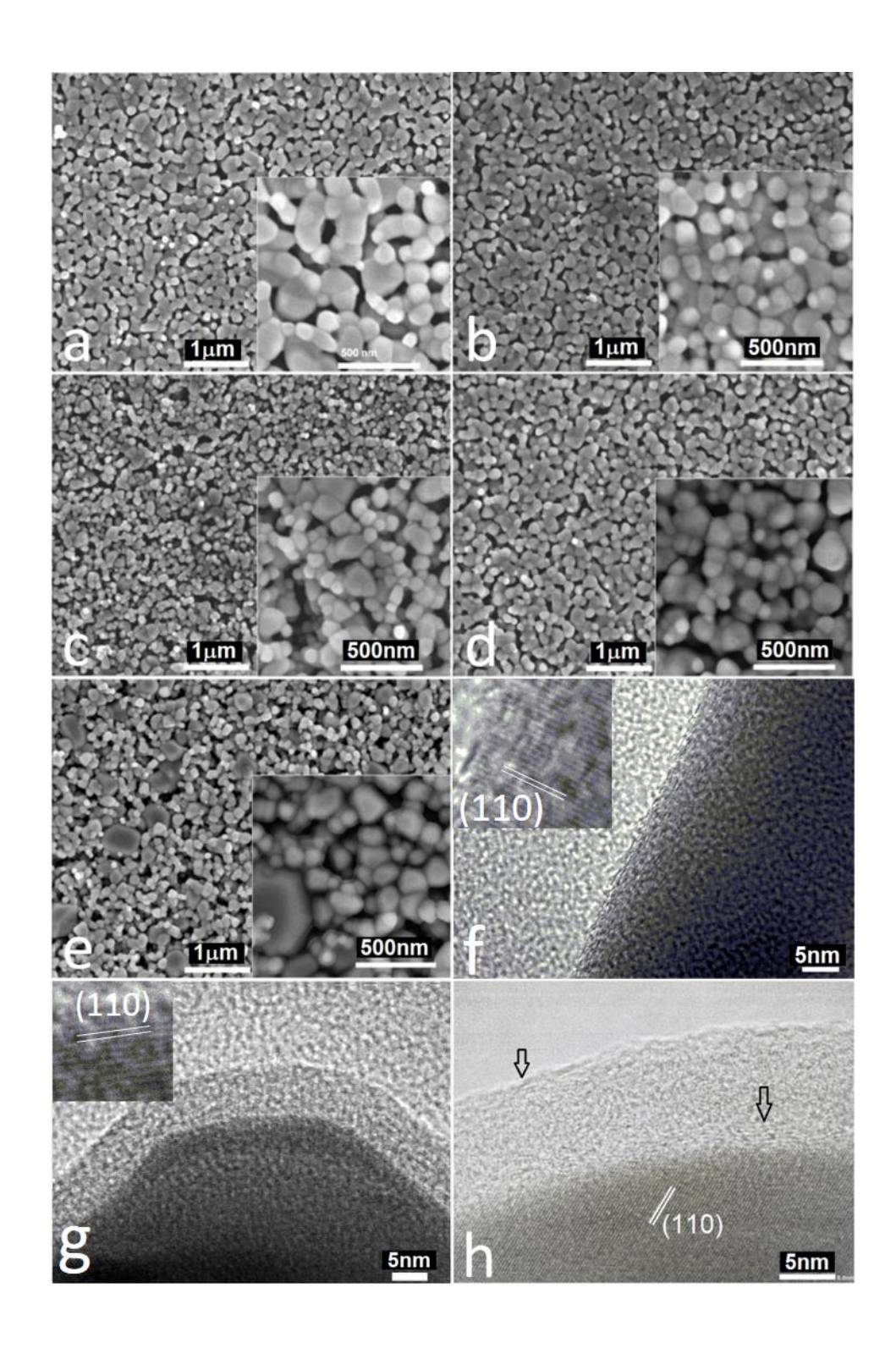


Figure 4. FESEM micrographs of upper surface of hematite photoanodes prepared with FeOOH powders synthesized with different levels of LA. (a) Fe<sub>2</sub>O<sub>3</sub> (0 g LA); (b) Fe<sub>2</sub>O<sub>3</sub>-FeO<sub>x</sub> (0.1 g LA); (c) Fe<sub>2</sub>O<sub>3</sub>-FeO<sub>x</sub> (0.2 g LA); (d) Fe<sub>2</sub>O<sub>3</sub>-FeO<sub>x</sub> (0.3 g LA); and (e) Fe<sub>2</sub>O<sub>3</sub>-FeO<sub>x</sub> (0.4 g LA). Insets show zoomed-in areas. TEM micrographs of material scraped from the hematite photoanodes: (f) Fe<sub>2</sub>O<sub>3</sub> (0 g LA); (g) Fe<sub>2</sub>O<sub>3</sub>-FeO<sub>x</sub> (0.2 g LA); and (h) Fe<sub>2</sub>O<sub>3</sub>-FeO<sub>x</sub> (0.4 g LA). In (f), (g) insets and (h) hematite 0.25 nm (110) lattice spacings are shown. Graphitic carbon layers between crystalline hematite and amorphous FeO<sub>x</sub> and trace surface carbon are arrowed in (h).

## 3.3. X-ray Photoelectron Spectroscopy (XPS) analysis.

Figure S5a shows a full XPS survey of a representative  $Fe_2O_3$ - $FeO_x$  (0.2g LA) sample showing iron, oxygen and carbon peaks. The C 1s band for every prepared hematite sample is shown in Figure S5b. Carbon is ubiquitous and adventitious carbon gave a significant C 1s peak centered at 285 eV for the  $Fe_2O_3$  (0g LA) sample. However, the intensity of this band increased with increasing precursor LA content indicating presence of additional carbon in the final  $Fe_2O_3$ - $FeO_x$  photoanode sample surface. The O 1s peak was composed of two bands due to lattice O at 529.7eV and surface hydroxyl at 531.4eV. With increasing LA use, a reduction in peak level of lattice O was observed in comparison to the height of the surface hydroxyl band, indicating the presence of (less oxidized)  $Fe^{2+}$  and/or a higher proportion of the contribution from hydroxyl bands (Figure S5c).  $^{46,47}$  The Fe 2p showed spin orbit component at  $2p_{1/2} \sim 724.2eV$  and  $2p_{3/2}$  at  $\sim 710.8eV$  consistent with  $Fe_2O_3$  (Figure S5d). At the highest LA precursor level a trace peak at 716.2 eV associated with  $Fe^{2+}$  is present. The difference in binding energy [ $\Delta$ (BE)] altered from 13.3 to 13.6 with increasing LA component of precursor.  $^{48,49}$ 

#### 3.4 Energy dispersive X-ray Spectroscopy (EDXS).

EDXS mapping carried out during the TEM showed the coating to be composed of iron oxide only; carbon detection was not reliable and other elements were at background levels (Figure S6). EDXS was also conducted at low magnification SEM (~250μm diameter EDXS collection area) and elemental composition measured. Oxygen, iron, tin and trace potassium (from trace levels of remnant electrolyte) were detected (Figure S7). For the Fe<sub>2</sub>O<sub>3</sub>-FeO<sub>x</sub> (0.4g LA) a high Sn level was measured. This was most likely due to the presence of pores exposing FTO glass surface (Table S2).

Taking everything into consideration, the crystalline  $\gamma/\beta$ -FeOOH in LA absence converted upon deposition and heating to sharp well-defined hematite crystals, while more amorphous and surface disordered  $\alpha$ -phase-rich FeOOH prepared with LA presence dehydrated to hematite crystals with an amorphous FeO<sub>x</sub> coating upon heating. Overall, during the short heating step a major morphological alteration from rods/amorphous material into crystalline or crystalline/amorphous blocks took place.

## 3.5. PEC performance.

Photocurrent density performances of hematite photoanodes prepared with different amounts of LA were measured with linear sweep voltammetry (LSV) under chopped simulated sunlight (100 mWcm<sup>-2</sup>, with an AM1.5G filter) (Figure 5a,b). A photocurrent of 0.32 mA cm<sup>-2</sup> was obtained at 1.23 V<sub>RHE</sub> for Fe<sub>2</sub>O<sub>3</sub> (0 g LA) photoanode, typical of hematite formed from precursor solution coatings and without oxygen evolution electrocatalysts such as FeOOH or cobalt phosphate.<sup>9,50,51</sup> On addition of LA to the FeOOH precursor preparations, photocurrent of final photoanodes increased up to a maximum of 1.39 mA cm<sup>-2</sup> [Fe<sub>2</sub>O<sub>3</sub>-FeO<sub>x</sub> (0.2 g LA)] then decreased back to 0.61 mA cm<sup>-2</sup> [Fe<sub>2</sub>O<sub>3</sub>-FeO<sub>x</sub> (0.4 g LA)], both at 1.23 V<sub>RHE</sub> (Figure 5a,c).

Surface activity was determined using CV measurements of the samples over 20-200mVs<sup>-1</sup> sweep rates (Figure S8). At lower sweep rate the applied charge had time to dissipate away. With increasing rate, an increasing charge density at the surface was measured over the anodic/cathodic scans. The slopes of the current density vs. scan rate can be related to the double layer capacitance  $(C_{dl})$  directly proportional to the ECSA (Figure 5b). The results indicate that the Fe<sub>2</sub>O<sub>3</sub>-FeOx (0.2g LA) photoanode possesses the largest electrochemically active surface ( $C_{dl} = 0.074 \text{ mF cm}^{-2}$ ), followed by Fe<sub>2</sub>O<sub>3</sub>-FeO<sub>x</sub> - 0.3 g, - 0.1 g, - 0 g and lastly - 0.4g LA samples. Figure 5c compares photocurrents and ECSA values showing they follow the same rising and falling trend with increasing LA presence in FeOOH precursor preparation. The photocurrent obtained with Fe<sub>2</sub>O<sub>3</sub>-FeO<sub>x</sub> (0.4g LA) sample was however higher than what it would be expected considering its lowest  $C_{dl}$ . This can be ascribed to the presence of trace graphitic carbon observed by TEM at the α-Fe<sub>2</sub>O<sub>3</sub>-FeO<sub>x</sub> interface increasing electrical conductivity. Table 1 shows hematite particle sizes measured on the surface by FESEM, calculated surface areas, and photocurrent densities measured at 1.23 V<sub>RHE</sub>. Photoactivity was related with particle size and optimal photocurrent occurred for Fe<sub>2</sub>O<sub>3</sub>-FeO<sub>x</sub> (0.2g LA) which coincides with the smallest hematite particle size and a medium thickness of amorphous FeO<sub>x</sub> coating. Overall, these results show there exists an optimal addition of LA to the FeOOH precursor preparation to achieve the best hematite photoanode performance.

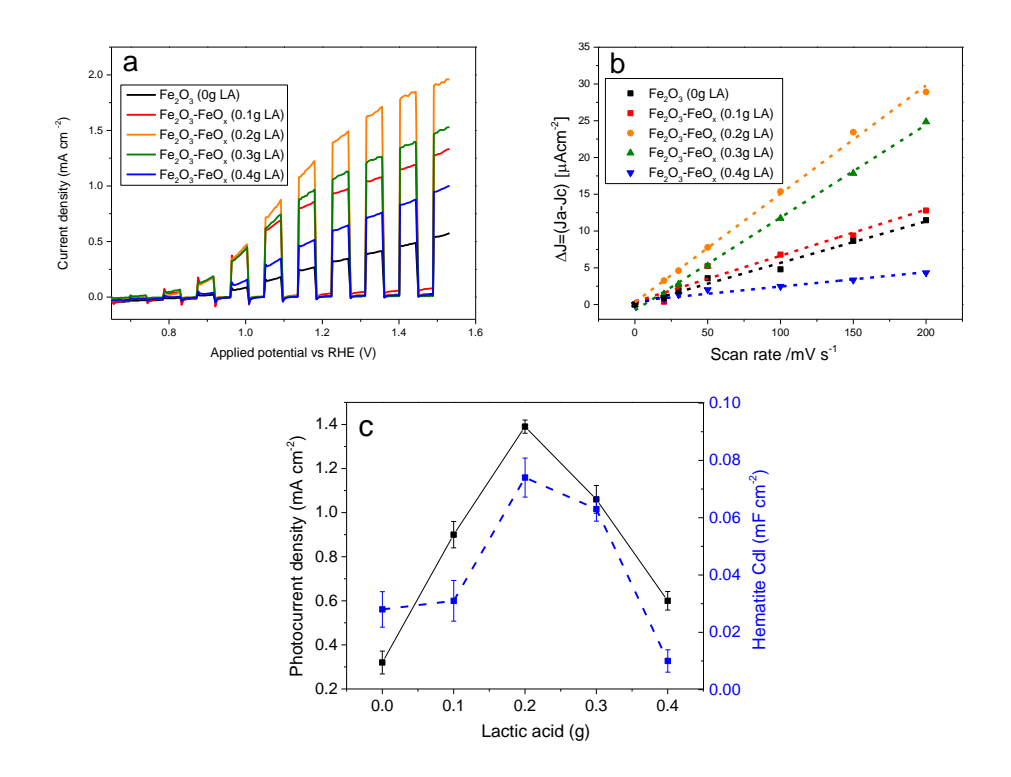


Figure 5. Electrochemical characterization of hematite photoanodes prepared with FeOOH powders synthesized with different levels of LA. (a) Current density as a function of applied potential (J-V) carried out in 1 M KOH electrolyte under chopped simulated sunlight (AM1.5G, 100 mW cm<sup>-2</sup>). (b) Scan rate dependence of current densities ( $\Delta J$ ) for the calculation of ECSA values ( $C_{dl}$ ). (c) Photocurrent density (solid line) at 1.23 V<sub>RHE</sub> and ECSA values  $C_{dl}$  (dashed line) as a function of LA used in synthesis procedure. Error bars denote photocurrent and  $C_{dl}$  standard deviation of three replicate samples.

Table 1. Characteristics of hematite photoanodes prepared with FeOOH powders synthesized with different levels of LA: particle size (and std deviation) on the surface analyzed by FESEM; surface area (assuming spherical particles of previous sizes and hematite density of 5.26 g/cm<sup>3</sup>); measured ECSA values ( $C_{dl}$ ) (and std deviation); FeO<sub>x</sub> amorphous overlayer thickness analyzed by TEM; and corresponding measured photocurrent (J) at 1.23V<sub>RHE</sub> under simulated sunlight (back illumination).

Sample	Particle size	Surface	ECSA C <sub>dl</sub>	FeO <sub>x</sub>	J
	(nm)	area	$(mF cm^{-2})$	(nm)	$(mA cm^{-2})$
		$(m^2/g)$			
$Fe_2O_3$ (0g LA)	165 (45)	6.9	0.028(0.0062)	0	0.32
$Fe_2O_3$ - $FeO_x(0.1g LA)$	100 (30)	11.4	0.031(0.0071)		0.90
$Fe_2O_3$ - $FeO_x$ (0.2g LA)	95 (25)	12.0	0.074(0.0068)	5-10	1.39
$Fe_2O_3$ - $FeO_x(0.3g LA)$	140 (54)	8.2	0.063(0.0042)		1.06
$Fe_2O_3$ - $FeO_x$ (0.4g LA)	168 (125)	6.8	0.010(0.0039)	10-20	0.60

Back illumination was used as this eliminates PEC variation due to sample thicknesses. Moreover, it also gave higher photocurrents than front one in all cases, indicating these porous hematite films have sufficient thickness to measure highest photocurrent possible for each condition assessed.<sup>52</sup> Depositions and measurements were repeated more than five times showing reproducible trends and results (see example at optimal Fe<sub>2</sub>O<sub>3</sub>-FeO<sub>x</sub> (0.2 g LA) in Figure S9, mean=1.35 ((σ=0.06) mA cm<sup>-2</sup> at 1.23 V<sub>RHE</sub>). Photostability under 1-sun chopped illumination for a total of 2.5 h showed a decrease of 3% over the initial 20 min, followed by a constant photocurrent density, indicating high stability of the hematite film (Figure S10).

Intrinsic water oxidation capability of the anode surfaces was assessed measuring J-V curves under dark conditions at elevated applied potential up to 2.0 V<sub>RHE</sub> (Figure 6a).<sup>53</sup> Tafel plots showed that the lowest onset potential and a clearly higher current density occurred with the Fe<sub>2</sub>O<sub>3</sub>-FeO<sub>x</sub> (0.2g LA) anode (Figure 6b). The Fe<sub>2</sub>O<sub>3</sub> (0g LA) sample showed next lowest onset

(Figure 6b). These results further confirmed that the photoanodes with an optimal amorphous FeO<sub>x</sub> layer thickness and surface area can obtain higher currents for water oxidation.

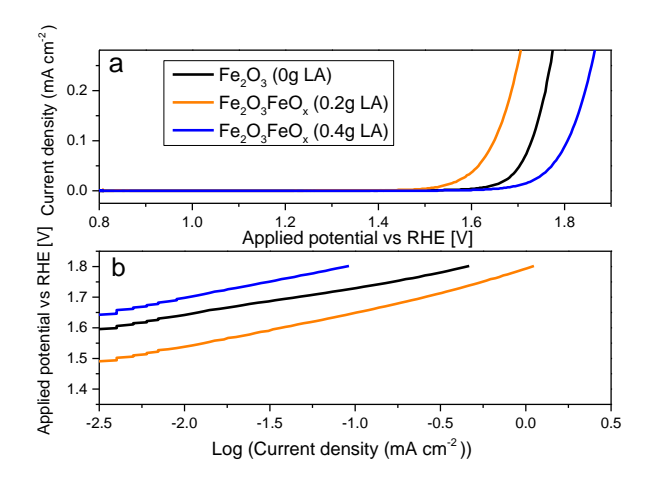


Figure 6. (a) Current density as a function of applied potential (*J-V*) of hematite photoanodes prepared with FeOOH powders synthesized with different levels of LA, under dark conditions in 1M KOH, showing intrinsic water oxidation ability. (b) Corresponding Tafel plots.

#### 3.6. Hole scavenger measurements.

Sacrificial reagents such as  $H_2O_2$  can be used as a hole scavenger to elucidate electron-hole surface recombination photocurrent losses, that among other factors hamper reaching the hematite photocurrent theoretical limit (12.5 mA cm<sup>-2</sup>).<sup>17</sup> Measuring photocurrents with and without  $H_2O_2$  in the same electrolyte (KOH), charge transfer efficiencies ( $\eta_{ct}$ ) can be calculated by the ratio of photocurrent densities (Table 2). In the presence of  $H_2O_2$ , the photocurrent density of the Fe<sub>2</sub>O<sub>3</sub> (0g LA) sample was higher at all potentials and more than doubled at 1.23  $V_{RHE}$  showing the high degree of surface recombination losses of photocurrent in 1M KOH electrolyte ( $\eta_{ct}$  of 49% at 1.23  $V_{RHE}$ , Figure 7 and Table 2). However, for Fe<sub>2</sub>O<sub>3</sub>-FeO<sub>x</sub> (0.2 g and 0.4 g LA) samples, higher charge transfer efficiencies were observed, for example  $\eta_{ct} \sim 80$  % at 1.23  $V_{RHE}$ . We ascribe this higher efficiency to the presence of the amorphous

FeO<sub>x</sub> coating, acting as an O<sub>2</sub> evolution electrocatalyst. Comparison of  $\eta_{ct}$  for Fe<sub>2</sub>O<sub>3</sub> (0 g LA) photoanode against Fe<sub>2</sub>O<sub>3</sub>-FeO<sub>x</sub> (0.2 g and 0.4 g LA) photoanodes shows some advantage at 0.95 V<sub>RHE</sub> (from 13.5 to 17.6 and 16.4 %  $\eta_{ct}$ , resp.). However, enhancements became even more significant at 1.23 V<sub>RHE</sub> (from 49 to ~80%  $\eta_{ct}$ ). This higher activity at higher potentials indicate the amorphous FeO<sub>x</sub> coating behaves as an FeOOH electrocatalyst, whose conductivity has been measured to increase substantially with stronger applied potentials in its pure form or mixed with other metals.<sup>54</sup> From XPS results we noticed intensified Sn 2p signals with higher LA addition, meaning FeO<sub>x</sub> could also be mixed with Sn.

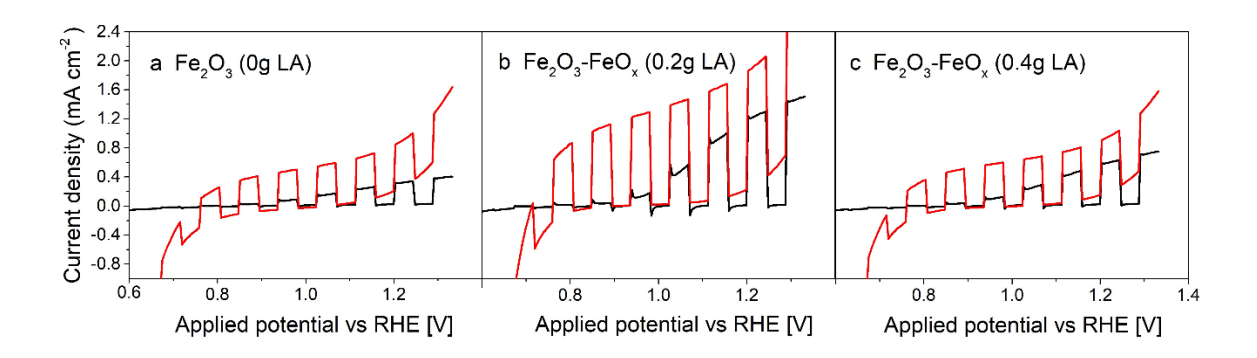


Figure 7. Hole scavenger measurements of hematite photoanodes prepared with FeOOH powders synthesized with different levels of LA. Current density as a function of applied potential under chopped simulated sunlight (AM1.5G, 100 mW cm<sup>-2</sup>). Electrolyte: 1 M KOH (black curve) and 1 M KOH containing 0.5 M H<sub>2</sub>O<sub>2</sub> (red curve). (a) Fe<sub>2</sub>O<sub>3</sub> (0 g LA); (b) Fe<sub>2</sub>O<sub>3</sub>-FeO<sub>x</sub> (0.2 g LA); and (c) Fe<sub>2</sub>O<sub>3</sub>-FeO<sub>x</sub> (0.4 g LA).

Table 2. Analysis of hole scavenger measurements of hematite photoanodes prepared with FeOOH powders synthesized with different levels of LA. Table includes photocurrent densities measured in different electrolytes and under different applied potentials and charge transfer efficiency ( $\eta_{ct}$  (%)) at applied voltages of 0.95 and 1.23  $V_{RHE}$ . Photocurrents in electrolytes with  $H_2O_2$  are corrected for the dark current observed.

	Sample	Fe <sub>2</sub> O <sub>3</sub> (0 g LA)		$Fe_2O_3$ - $FeO_x$ (0.2 g LA)		$Fe_2O_3$ - $FeO_x$ (0.4 g LA)	
•	Potential (V <sub>RHE</sub> )	0.95	1.23	0.95	1.23	0.95	1.23
-	J <sub>1 M KOH</sub>	0.07	0.31	0.21	1.23	0.10	0.59
	$\rm J_{1MKOH+0.5MH2O2}$	0.52	0.63	1.19	1.51	0.59	0.74
	η <sub>ct</sub> (%)	13.5	49.2	17.6	81.4	16.4	79.7

# 3.7. PEIS analysis.

To further understand the differences in the surface kinetics of photoanodes having different FeO<sub>x</sub> coating thickness, photo-electrochemical impedance spectroscopy (PEIS) was employed. Nyquist plots were obtained at different potentials in 1 M KOH and fitted using an equivalent circuit proposed by Klahr *et al.* for hematite (Figure 8a).<sup>55</sup> In this model, water oxidation is assumed to take place via surface states, which competes with surface charge recombination. The density of surface states is represented by the capacitor  $C_{ss}$ . The fitted  $C_{ss}$  values are shown in Figure 8b, where peak maxima were located at 0.9-1.0 V<sub>RHE</sub>, which coincide with the onset potential of hematite. Importantly, the  $C_{ss}$  of the Fe<sub>2</sub>O<sub>3</sub>-FeO<sub>x</sub> (0.2 and 0.4 g LA) photoanodes was much higher than that of Fe<sub>2</sub>O<sub>3</sub> (0 g LA) reference photoanode, which can be attributed to the presence of amorphous FeO<sub>x</sub> conductive coating observed by FESEM and TEM. Moreover, the  $C_{ss}$  of Fe<sub>2</sub>O<sub>3</sub>-FeO<sub>x</sub> (0.2 g LA) was double than that of Fe<sub>2</sub>O<sub>3</sub>-FeO<sub>x</sub> (0.4 g LA), in agreement with the largest electrochemical current densities and PEC photocurrents observed (Figure 5).

Therefore,  $C_{ss}$  values together with PEC results indicate the amorphous FeO<sub>x</sub> coating help store and shuttle photoinduced holes to the electrolyte, boosting photocurrents observed.

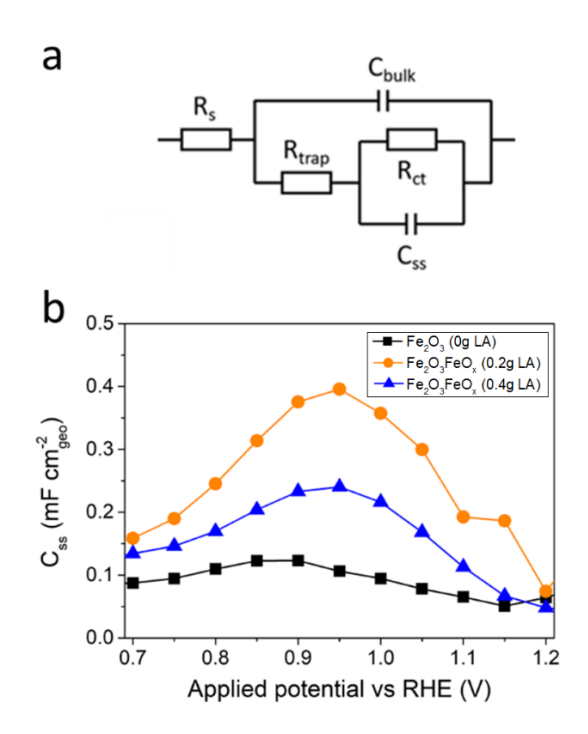


Figure 8. (a) Equivalent circuit used for fitting PEIS data. (b) PEIS analysis. Surface state capacitances ( $C_{ss}$ ) calculated as a function of applied potential for hematite photoanodes prepared with FeOOH powders synthesized with different levels of LA. Conditions: 1 M KOH electrolyte, simulated sunlight (AM1.5G, 100 mW cm<sup>-2</sup>).

# 3.8. Light-absorption and IPCE.

UV-visible spectroscopy was used to measure light absorbance of prepared photoanodes and confirm the amorphous  $FeO_x$  layer does not affect the band gap (Figure S11a). A Tauc plot was applied to determine direct and indirect band gaps.<sup>56</sup> Direct band gaps were located at  $E_g$  2.05-2.08eV (~600nm) and indirect around  $E_g$  2.04eV (608nm), both in accordance with submicron sized hematite (Figure S11b,c).<sup>56</sup> Light absorption properties and band-gap energies

of hematite photoanodes were also studied by IPCE measurements (Figure 9). The IPCE curves were consistent with photocurrent density results: the Fe<sub>2</sub>O<sub>3</sub> (0 g LA) gave 6% maximum IPCE, Fe<sub>2</sub>O<sub>3</sub>-FeO<sub>x</sub> (0.4 g LA) 13% and Fe<sub>2</sub>O<sub>3</sub>-FeO<sub>x</sub> (0.2 g LA) a marked improved IPCE maximum efficiency of 23%. The low IPCE for photoanodes lacking an FeO<sub>x</sub> amorphous coating further suggests the majority of electron-hole pairs recombine and thus no significant free charge carriers are transferred to the electrolyte. However, in the presence of an FeOx amorphous coating behaving as an FeOOH electrocatalysts, higher IPCE efficiencies are obtained due to a better utilization of the photoinduced charges.

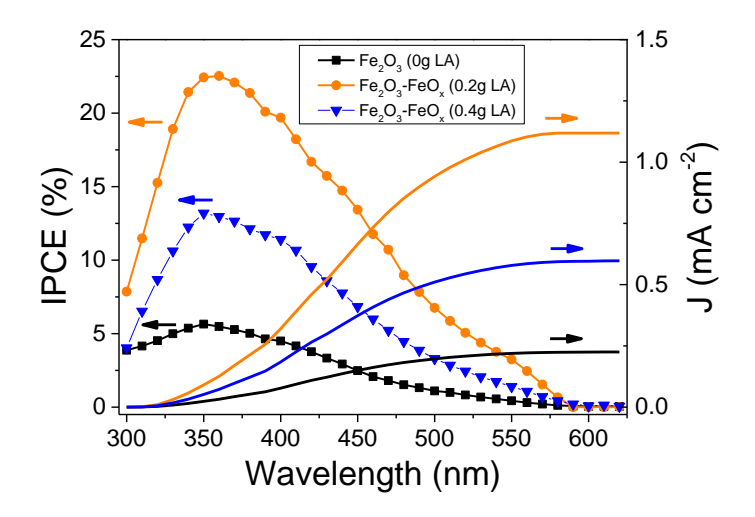
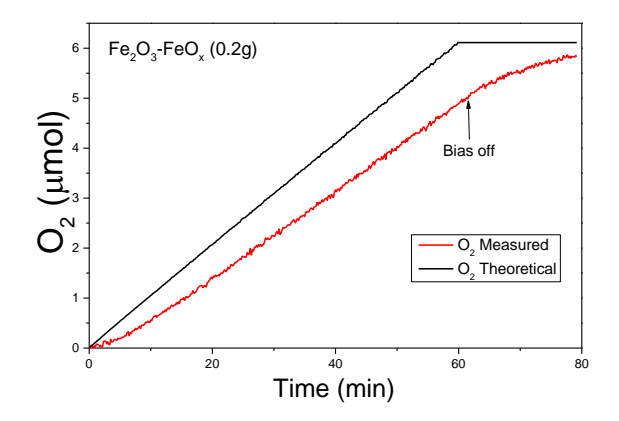


Figure 9. IPCE curves of hematite photoanodes prepared with FeOOH powders synthesized with different levels of LA. Integrated photocurrent density profiles with AM1.5G solar spectrum are also shown on right y-axis.

## 3.9 Faradaic efficiency measurement.

 $O_2$  evolution and photocurrent measurements were performed on the best photoanode  $[Fe_2O_3\text{-}FeO_x~(0.2g~LA)]$  at 1.23  $V_{RHE}$  under 1 sun illumination (Figure 10). The amount of  $O_2$  in the headspace of a gas-tight PEC cell increased linearly with time during irradiation. Using

the photocurrent–time curve obtained (Figure S12), the theoretical amount of O<sub>2</sub> expected for a water oxidation reaction with 100% faradaic efficiency was calculated and also represented in Figure 10. Comparison between values indicated that Fe<sub>2</sub>O<sub>3</sub>-FeO<sub>x</sub> (0.2 g LA) photoanode has a Faradaic efficiency of approx. 70% (details of calculations are shown in the SI). This level is typical of high performing hematite photoanodes and is consistent with a high level of the photogenerated charges being employed in water splitting and hydrogen/oxygen production.<sup>9</sup>



**Figure 10.** Amount of O<sub>2</sub> gas evolved at 1.23V<sub>RHE</sub> under simulated sunlight (AM1.5G, 100 mW cm<sup>-2</sup>) using the best performing Fe<sub>2</sub>O<sub>3</sub>-FeO<sub>x</sub> (0.2g LA) sample photoanode. The amount of O<sub>2</sub> quantified with a fluorescence probe is represented by the red line, whereas the theoretical amount of O<sub>2</sub> calculated assuming a 100% faradaic efficiency is shown by the black line.

# Conclusions

We investigated the effect of the preparation of FeOOH precursors have on final hematite photoanodes prepared by a simple doctor-blading deposition and heating step. We found that addition of lactic acid to the formation of FeOOH lepidocrocite nanorods changed its crystallinity and type of crystal phase, obtaining instead amorphous and goethite FeOOH.

When used as a precursor for the preparation of films on a conductive support, the amorphous and goethite FeOOH resulted in the simultaneous formation of particulate hematite films with particles covered with a conductive amorphous FeO<sub>x</sub> coating. The thickness of this FeO<sub>x</sub> coating with excellent coverage and interface quality was effectively controlled by the addition of lactic acid to the FeOOH precursor preparation, being optimal at ~3:1 Fe:LA ratio. Such FeO<sub>x</sub> coating had a profound effect on the photoelectrochemical properties of films, producing a more than four-fold enhancement in photocurrent density, from 0.32 to 1.39 mA cm<sup>-2</sup> at 1.23 V<sub>RHE</sub> under simulated sunlight. Detailed characterization demonstrated that the photocurrent enhancement resulted from an increase in both electrochemically-active surface area and surface states capacitance. Importantly, all the characterization indicated that the formed amorphous FeOx coating is of equivalent catalytic behavior to the very active FeOOH electrocatalyst. Like many successful electrocatalysts, it increased charged transfer efficiency by significantly reducing surface charge recombination. Finally, we found that an excess of lactic acid decreases surface area but this is partly compensated by graphitic carbon sheets trapped between the crystalline hematite and FeO<sub>x</sub> amorphous coating that increase conductivity and photoelectrochemical performance. Our findings have opened a new approach to produce more efficient hematite photoanodes with tuned semiconductorelectrolyte interface without extra steps of electrocatalyst addition and streamlined methodology. Further work to understand the mechanism of formation of the amorphous FeO<sub>x</sub> layer and the potential of this approach for other semiconductor types is currently under way.

ASSOCIATED CONTENT

**Supporting Information.** 

The Supporting Information is available free of charge on the ACS Publication website at

DOI: xxxxxx

Raman spectroscopy; Crystal structure of hematite and (110) plane; SEM cross sections of

hematite/FTO slides; TEM of hematite/FeO<sub>x</sub>; EDXS elemental mapping; XPS; Cyclic

Voltammetry curves; Repeat photocurrent measurements; Photoanode sample stability

measurement, UV-visible spectroscopy and Tauc plots, and Faradaic efficiency

measurements.

All data created during this research are openly available from the University of Bath data

archive at https://doi.org/10.15125/BATH-00599

**AUTHOR INFORMATION** 

**Corresponding Authors** 

Email: d.walsh2@bath.ac.uk

Email: s.eslava@bath.ac.uk

**Author Contributions** 

The manuscript was written through contributions of all authors. All authors have given

approval to the final version of the manuscript.

ACKNOWLEDGMENT

We thank the University of Bath Material and Chemical Characterisation Facility (MC2) for

assistance with SEM, TEM and Raman Analysis.

28

#### **FUNDING SOURCES**

XPS data collection was performed at the EPSRC National Facility for XPS ('HarwellXPS'), operated by Cardiff University and UCL, under contract No.PR16195. S. Eslava and D. Walsh acknowledge funding from EPSRC Grant EP/P008097/1 and M. Regue acknowledges funding Centre for Sustainable Chemical Technologies CDT EPSRC Grant EP/L016354/1.

#### **ABBREVIATIONS**

LA lactic acid; FESEM Field Emission Scanning Electron Microscopy; FTO fluoridated tin oxide; XPS X-ray photoelectron spectroscopy; ECSA electrochemically active surface area; PEIS photo-electrochemical impedance spectroscopy; IPCE Incident photon to current efficiency.

BRIEFS. We demonstrate the simultaneous synthesis of an amorphous iron oxide electrocatalyst on a hematite absorber layer for enhanced photoelectrochemical solar water oxidation.

## REFERENCES

- 1. BP Statistical Review of World Energy 2017 66th Edition; British Petroleum: 2017.
- 2. Miller, E. L., Photoelectrochemical water splitting. *Energy & Environmental Science* **2015,** *8*, 2809-2810.
- 3. Shi, Z.; Wen, X.; Guan, Z.; Cao, D.; Luo, W.; Zou, Z., Recent progress in photoelectrochemical water splitting for solar hydrogen production. *Annals of Physics* **2015**, *358*, 236-247.
- 4. Joy, J.; Mathew, J.; George, S. C., Nanomaterials for photoelectrochemical water splitting review. *International Journal of Hydrogen Energy* **2018**, *43*, 4804-4817.
- 5. Lin, Y.; Yuan, G.; Sheehan, S.; Zhou, S.; Wang, D., Hematite-based solar water splitting: challenges and opportunities. *Energy & Environmental Science* **2011**, *4*, 4862-4869.
- 6. Bora, D. K.; Braun, A.; Constable, E. C., "In rust we trust". Hematite the prospective inorganic backbone for artificial photosynthesis. *Energy & Environmental Science* **2013**, *6*, 407-425.
- 7. Itoh, K.; Bockris, J. O. M., Thin Film Photoelectrochemistry: Iron Oxide. *Journal of The Electrochemical Society* **1984**, *131*, 1266-1271.

- 8. Mishra, M.; Chun, D.-M., α-Fe<sub>2</sub>O<sub>3</sub> as a photocatalytic material: A review. *Applied Catalysis A: General* **2015**, *498*, 126-141.
- 9. Kim, J. Y.; Magesh, G.; Youn, D. H.; Jang, J.-W.; Kubota, J.; Domen, K.; Lee, J. S., Single-crystalline, wormlike hematite photoanodes for efficient solar water splitting. *Scientific Reports* **2013**, *3*, 2681.
- 10. Li, Y.; Guijarro, N.; Zhang, X.; Prévot, M. S.; Jeanbourquin, X. A.; Sivula, K.; Chen, H.; Li, Y., Templating Sol–Gel Hematite Films with Sacrificial Copper Oxide: Enhancing Photoanode Performance with Nanostructure and Oxygen Vacancies. *ACS Applied Materials & Interfaces* **2015**, *7*, 16999-17007.
- 11. Barreca, D.; Carraro, G.; Gasparotto, A.; Maccato, C.; Warwick, M. E. A.; Kaunisto, K.; Sada, C.; Turner, S.; Gönüllü, Y.; Ruoko, T.-P.; Borgese, L.; Bontempi, E.; Van Tendeloo, G.; Lemmetyinen, H.; Mathur, S., Fe2O3–TiO2 Nano-heterostructure Photoanodes for Highly Efficient Solar Water Oxidation. *Advanced Materials Interfaces* **2015**, *2*, 1500313.
- 12. Carraro, G.; Maccato, C.; Gasparotto, A.; Warwick, M. E. A.; Sada, C.; Turner, S.; Bazzo, A.; Andreu, T.; Pliekhova, O.; Korte, D.; Lavrenčič Štangar, U.; Van Tendeloo, G.; Morante, J. R.; Barreca, D., Hematite-based nanocomposites for light-activated applications: Synergistic role of TiO2 and Au introduction. *Solar Energy Materials and Solar Cells* **2017**, *159*, 456-466.
- 13. Singh, A. P.; Saini, N.; Mehta, B. R.; Carraro, G.; Barreca, D., Hematite Thin Film Photoanodes for Visible Light Water Photooxidation: Effects of Zn Doping and Hydrogen Treatment. *Journal of Nanoscience and Nanotechnology* **2017**, *17*, 8959-8966.
- 14. Sivula, K.; Zboril, R.; Le Formal, F.; Robert, R.; Weidenkaff, A.; Tucek, J.; Frydrych, J.; Grätzel, M., Photoelectrochemical Water Splitting with Mesoporous Hematite Prepared by a Solution-Based Colloidal Approach. *Journal of the American Chemical Society* **2010**, *132*, 7436-7444.
- 15. Sivula, K.; Le Formal, F.; Grätzel, M., Solar Water Splitting: Progress Using Hematite (α-Fe2O3) Photoelectrodes. *ChemSusChem* **2011**, *4*, 432-449.
- 16. Jeon, T. H.; Moon, G.-h.; Park, H.; Choi, W., Ultra-efficient and durable photoelectrochemical water oxidation using elaborately designed hematite nanorod arrays. *Nano Energy* **2017**, *39*, 211-218.
- 17. Tamirat, A. G.; Rick, J.; Dubale, A. A.; Su, W.-N.; Hwang, B.-J., Using hematite for photoelectrochemical water splitting: a review of current progress and challenges. *Nanoscale Horizons* **2016**, *1*, 243-267.
- 18. Zhong, D. K.; Cornuz, M.; Sivula, K.; Grätzel, M.; Gamelin, D. R., Photo-assisted electrodeposition of cobalt–phosphate (Co–Pi) catalyst on hematite photoanodes for solar water oxidation. *Energy & Environmental Science* **2011**, *4*, 1759-1764.
- 19. Qiu, Y.; Leung, S.-F.; Zhang, Q.; Hua, B.; Lin, Q.; Wei, Z.; Tsui, K.-H.; Zhang, Y.; Yang, S.; Fan, Z., Efficient Photoelectrochemical Water Splitting with Ultrathin films of Hematite on Three-Dimensional Nanophotonic Structures. *Nano Letters* **2014**, *14*, 2123-2129.
- 20. Mohapatra, S. K.; John, S. E.; Banerjee, S.; Misra, M., Water Photooxidation by Smooth and Ultrathin α-Fe2O3 Nanotube Arrays. *Chemistry of Materials* **2009**, *21*, 3048-3055.
- 21. Yang, J.; Wang, D.; Han, H.; Li, C., Roles of Cocatalysts in Photocatalysis and Photoelectrocatalysis. *Accounts of Chemical Research* **2013**, *46*, 1900-1909.
- 22. Hesari, M.; Mao, X.; Chen, P., Charge Carrier Activity on Single-Particle Photo(electro)catalysts: Toward Function in Solar Energy Conversion. *Journal of the American Chemical Society* **2018**, *140*, 6729-6740.

- 23. Warwick, M. E. A.; Barreca, D.; Bontempi, E.; Carraro, G.; Gasparotto, A.; Maccato, C.; Kaunisto, K.; Ruoko, T. P.; Lemmetyinen, H.; Sada, C.; Gönüllü, Y.; Mathur, S., Pt-functionalized Fe<sub>2</sub>O<sub>3</sub> photoanodes for solar water splitting: the role of hematite nano-organization and the platinum redox state. *Physical Chemistry Chemical Physics* **2015**, *17*, 12899-12907.
- 24. Badia-Bou, L.; Mas-Marza, E.; Rodenas, P.; Barea, E. M.; Fabregat-Santiago, F.; Gimenez, S.; Peris, E.; Bisquert, J., Water Oxidation at Hematite Photoelectrodes with an Iridium-Based Catalyst. *The Journal of Physical Chemistry C* **2013**, *117*, 3826-3833.
- 25. Zhang, J.; García-Rodríguez, R.; Cameron, P.; Eslava, S., Role of cobalt—iron (oxy)hydroxide (CoFeOx) as oxygen evolution catalyst on hematite photoanodes. *Energy & Environmental Science* **2018**, *11*, 2972-2984.
- 26. McAlpin, J. G.; Surendranath, Y.; Dincă, M.; Stich, T. A.; Stoian, S. A.; Casey, W. H.; Nocera, D. G.; Britt, R. D., EPR Evidence for Co(IV) Species Produced During Water Oxidation at Neutral pH. *Journal of the American Chemical Society* **2010**, *132*, 6882-6883.
- 27. Louie, M. W.; Bell, A. T., An Investigation of Thin-Film Ni–Fe Oxide Catalysts for the Electrochemical Evolution of Oxygen. *Journal of the American Chemical Society* **2013**, *135*, 12329-12337.
- 28. McCrory, C. C. L.; Jung, S.; Peters, J. C.; Jaramillo, T. F., Benchmarking Heterogeneous Electrocatalysts for the Oxygen Evolution Reaction. *Journal of the American Chemical Society* **2013**, *135*, 16977-16987.
- 29. Bowmer, C. T.; Hooftman, R. N.; Hanstveit, A. O.; Venderbosch, P. W. M.; van der Hoeven, N., The ecotoxicity and the biodegradability of lactic acid, alkyl lactate esters and lactate salts. *Chemosphere* **1998**, *37*, 1317-1333.
- 30. Blanco-Andujar, C.; Ortega, D.; Pankhurst, Q. A.; Thanh, N. T. K., Elucidating the morphological and structural evolution of iron oxide nanoparticles formed by sodium carbonate in aqueous medium. Journal of Materials Chemistry 2012, 22, 12498-12506.
- 31. Park, M. S.; Walsh, D.; Zhang, J.; Kim, J. H.; Eslava, S., Efficient hematite photoanodes prepared by hydrochloric acid-treated solutions with amphiphilic graft copolymer. *Journal of Power Sources* **2018**, *404*, 149-158.
- 32. Bard, A. J.; Faulkner, L. R., *Electrochemical Method: Fundamentals and Applications*. Second Edition ed.; John Wiley and Sons: New York: 2001.
- 33. Kang, B. K.; Han, G. S.; Baek, J. H.; Lee, D. G.; Song, Y. H.; Kwon, S. B.; Cho, I. S.; Jung, H. S.; Yoon, D. H., Nanodome Structured BiVO/GaOxN<sub>1-x</sub> Photoanode for Solar Water Oxidation. *Advanced Materials Interfaces* **2017**, *4*, 1700323.
- 34. Duan, Y.; Zhou, S.; Chen, Z.; Luo, J.; Zhang, M.; Wang, F.; Xu, T.; Wang, C., Hierarchical TiO2 nanowire/microflower photoanode modified with Au nanoparticles for efficient photoelectrochemical water splitting. *Catalysis Science & Technology* **2018**, *8*, 1395-1403.
- 35. Regue, M.; Armstrong, K.; Walsh, D.; Richards, E.; Johnson, A. L.; Eslava, S., Mo-doped TiO<sub>2</sub> photoanodes using [Ti<sub>4</sub>Mo<sub>2</sub>O<sub>8</sub>(OEt)<sub>10</sub>]<sub>2</sub> bimetallic oxo cages as a single source precursor. *Sustainable Energy & Fuels* **2018**.
- 36. Dotan, H.; Sivula, K.; Gratzel, M.; Rothschild, A.; Warren, S. C., Probing the photoelectrochemical properties of hematite (α-Fe<sub>2</sub>O<sub>3</sub>) electrodes using hydrogen peroxide as a hole scavenger. *Energy & Environmental Science* **2011**, *4*, 958-964.
- 37. J Chemistry of Iron Hydroxides and Iron Oxides. In *Developments in Petroleum Science*, Littmann, W., Ed. Elsevier: 1988; Vol. 24, pp 204-205.
- 38. Thomas, L. A.; Dekker, L.; Kallumadil, M.; Southern, P.; Wilson, M.; Nair, S. P.; Pankhurst, Q. A.; Parkin, I. P., Carboxylic acid-stabilised iron oxide nanoparticles for use in magnetic hyperthermia. *Journal of Materials Chemistry* **2009**, *19*, 6529-6535.

- 39. Palanikumar, S.; Kannammal, L.; Meenarathi, B.; Anbarasan, R., Effect of folic acid decorated magnetic fluorescent nanoparticles on the sedimentation of starch molecules. *International Nano Letters* **2014**, *4*, 104.
- 40. Xiao, F.; Li, W.; Fang, L.; Wang, D., Synthesis of akageneite (beta-FeOOH)/reduced graphene oxide nanocomposites for oxidative decomposition of 2-chlorophenol by Fentonlike reaction. *Journal of Hazardous Materials* **2016**, *308*, 11-20.
- 41. Hanesch, M., Raman spectroscopy of iron oxides and (oxy)hydroxides at low laser power and possible applications in environmental magnetic studies. *Geophysical Journal International* **2009**, *177*, 941-948.
- 42. de Faria, D. L. A.; Lopes, F. N., Heated goethite and natural hematite: Can Raman spectroscopy be used to differentiate them? *Vibrational Spectroscopy* **2007**, *45*, 117-121.
- 43. Santos-Carballal, D.; Du, Z.; King, H. E.; de Leeuw, N. H., A computational study of the interaction of organic surfactants with goethite  $\alpha$ -FeO(OH) surfaces. *RSC Advances* **2016**, *6*, 91893-91903.
- 44. Kment, S.; Schmuki, P.; Hubicka, Z.; Machala, L.; Kirchgeorg, R.; Liu, N.; Wang, L.; Lee, K.; Olejnicek, J.; Cada, M.; Gregora, I.; Zboril, R., Photoanodes with Fully Controllable Texture: The Enhanced Water Splitting Efficiency of Thin Hematite Films Exhibiting Solely (110) Crystal Orientation. *ACS Nano* **2015**, *9*, 7113-7123.
- 45. Zhang, X.; Cao, C.; Bieberle-Hütter, A., Orientation Sensitivity of Oxygen Evolution Reaction on Hematite. *The Journal of Physical Chemistry C* **2016**, *120*, 28694-28700.
- 46. Deng, J.; Lv, X.; Gao, J.; Pu, A.; Li, M.; Sun, X.; Zhong, J., Facile synthesis of carbon-coated hematite nanostructures for solar water splitting. *Energy & Environmental Science* **2013**, *6*, 1965-1970.
- 47. McIntyre, N. S.; Zetaruk, D. G., X-ray photoelectron spectroscopic studies of iron oxides. *Analytical Chemistry* **1977**, *49*, 1521-1529.
- 48. Cerrato, J. M.; Hochella, M. F.; Knocke, W. R.; Dietrich, A. M.; Cromer, T. F., Use of XPS to Identify the Oxidation State of Mn in Solid Surfaces of Filtration Media Oxide Samples from Drinking Water Treatment Plants. *Environmental Science & Technology* **2010**, *44*, 5881-5886.
- 49. Carraro, G.; Gasparotto, A.; Maccato, C.; Bontempi, E.; Barreca, D., PECVD of Hematite Nanoblades and Nanocolumns: Synthesis, Characterization, and Growth Model *Chemical Vapor Deposition* **2015**, *21*, 294-299.
- 50. Su, J.; Wang, J.; Liu, C.; Feng, B.; Chen, Y.; Guo, L., On the role of metal atom doping in hematite for improved photoelectrochemical properties: a comparison study. *RSC Advances* **2016**, *6*, 101745-101751.
- 51. Vaalma, C.; Buchholz, D.; Weil, M.; Passerini, S., A cost and resource analysis of sodium-ion batteries. *Nature Reviews Materials* **2018**, *3*, 18013.
- 52. Hammond, O. S.; Eslava, S.; Smith, A. J.; Zhang, J.; Edler, K. J., Microwave-assisted deep eutectic-solvothermal preparation of iron oxide nanoparticles for photoelectrochemical solar water splitting. *Journal of Materials Chemistry A* **2017**, *5*, 16189-16199.
- 53. Xie, J.; Liu, W.; Xin, J.; Lei, F.; Gao, L.; Qu, H.; Zhang, X.; Xie, Y., Dual Effect in Fluorine-Doped Hematite Nanocrystals for Efficient Water Oxidation. *ChemSusChem* **2017**, *10*, 4465-4471.
- 54. Burke, M. S.; Kast, M. G.; Trotochaud, L.; Smith, A. M.; Boettcher, S. W., Cobalt—Iron (Oxy)hydroxide Oxygen Evolution Electrocatalysts: The Role of Structure and Composition on Activity, Stability, and Mechanism. *Journal of the American Chemical Society* **2015**, *137*, 3638-3648.

- 55. Klahr, B.; Gimenez, S.; Fabregat-Santiago, F.; Bisquert, J.; Hamann, T. W., Electrochemical and photoelectrochemical investigation of water oxidation with hematite electrodes. *Energy & Environmental Science* **2012**, *5*, 7626-7636.
- 56. Tauc, J.; Grigorovici, R.; Vancu, A., Optical Properties and Electronic Structure of Amorphous Germanium. *physica status solidi (b)* **1966,** *15*, 627-637.
- 57. Wang, H.; Turner, J. A., Characterization of Hematite Thin Films for Photoelectrochemical Water Splitting in a Dual Photoelectrode Device. *Journal of The Electrochemical Society* **2010**, *157*, F173-F178.